AGU PUBLICATIONS

Global Biogeochemical Cycles

RESEARCH ARTICLE
10.1002/2014GB004813

Key Points:
- Equilibration efficiency relates surface residence time, gas exchange timescale
- Regions of low equilibration efficiency favor disequilibrium
- Gas exchange timescale largely set by mixed layer depth

Correspondence to:
D. C. Jones,
dannes@bas.ac.uk

Citation:
Jones, D. C., T. Ito, Y. Takano, and W.-C. Hsu (2014), Spatial and seasonal variability of the air-sea equilibration timescale of carbon dioxide, *Global Biogeochem. Cycles*, *28*, 1163–1178, doi:10.1002/2014GB004813.

Received 22 JAN 2014
Accepted 4 OCT 2014
Accepted article online 8 OCT 2014
Published online 5 NOV 2014

Spatial and seasonal variability of the air-sea equilibration timescale of carbon dioxide

Daniel C. Jones[1,2], Takamitsu Ito[2], Yohei Takano[2], and Wei-Ching Hsu[2,3]

[1]British Antarctic Survey, NERC, Cambridge, UK, [2]School of Earth and Atmospheric Sciences, Georgia Institute of Technology, Atlanta, Georgia, USA, [3]Department of Oceanography, Texas A&M University, College Station, Texas, USA

Abstract The exchange of carbon dioxide between the ocean and the atmosphere tends to bring waters within the mixed layer toward equilibrium by reducing the partial pressure gradient across the air-water interface. However, the equilibration process is not instantaneous; in general, there is a lag between forcing and response. The timescale of air-sea equilibration depends on several factors involving the depth of the mixed layer, wind speed, and carbonate chemistry. We use a suite of observational data sets to generate climatological and seasonal composite maps of the air-sea equilibration timescale. The relaxation timescale exhibits considerable spatial and seasonal variations that are largely set by changes in mixed layer depth and wind speed. The net effect is dominated by the mixed layer depth; the gas exchange velocity and carbonate chemistry parameters only provide partial compensation. Broadly speaking, the adjustment timescale tends to increase with latitude. We compare the observationally derived air-sea gas exchange timescale with a model-derived surface residence time and a data-derived horizontal transport timescale, which allows us to define two nondimensional metrics of equilibration efficiency. These parameters highlight the tropics, subtropics, and northern North Atlantic as regions of inefficient air-sea equilibration where carbon anomalies are relatively likely to persist. The efficiency parameters presented here can serve as simple tools for understanding the large-scale persistence of air-sea disequilibrium of CO_2 in both observations and models.

1. Introduction

The ocean is by far the largest reservoir of carbon dioxide in the climate system, containing approximately 50 times more carbon molecules than the atmospheric reservoir. The exchange of carbon between the atmosphere and the ocean affects the relative buildup of anthropogenic carbon between the two stores, with implications for radiative transfer in the atmosphere and carbonate chemistry in the ocean. In a climatological sense, the exchange of carbon dioxide between the surface ocean and the lower atmosphere occurs on annual timescales, significantly slower than nonreactive gases (e.g., N_2O, dimethyl sulfide, and O_2) due to the buffering effect of carbonate chemistry [*Broecker and Peng*, 1974]. The relative slowness of air-sea carbon exchange may allow surface waters to subduct into the interior ocean before they can fully equilibrate with the overlying atmosphere. The subduction of partially equilibrated waters can significantly modulate the efficiency of oceanic carbon pumps [*Toggweiler et al.*, 2003a, 2003b; *Ito and Follows*, 2013]. Significant perturbations occur to the surface carbon balance on seasonal and shorter timescales, including (i) temperature-induced solubility changes, (ii) phytoplankton blooms, and (iii) upwelling and entrainment of subsurface waters. Air-sea equilibration cannot catch up with these relatively fast processes, and the mismatch produces significant fluctuations in the partial pressure of carbon dioxide (pCO_2) [*Takahashi et al.*, 2009].

Oceanic uptake of anthropogenic carbon primarily depends on the rate at which the surface waters are subducted into the main thermocline, where the majority of anthropogenic carbon is stored [*Sarmiento and Sundquist*, 1992; *Sabine et al.*, 2004; *Gruber et al.*, 1996]. While the gas transfer coefficient is not likely the dominant factor controlling the global uptake of anthropogenic carbon, it can alter regional-scale carbon uptake where the mixed layer is relatively deep and the surface waters are only partially equilibrated, such as in the Subantarctic region [*Ito et al.*, 2004]. Under such conditions, the degree of equilibration can impact regional carbon uptake.

The equilibrium concentration of dissolved inorganic carbon (C_{Sat}) is a function of the temperature (T), salinity (S), alkalinity (Alk), and pCO_2 of the overlying atmosphere. The presence of nonzero carbon fluxes

implies that the surface ocean is not normally in equilibrium with the atmosphere on regional scales [*Takahashi et al.*, 2009]. We can define carbon disequilibrium (ΔC) as

$$\Delta C = C - C_{sat}(T, S, \mathrm{Alk}, pCO_2), \tag{1}$$

where C is the carbon concentration of a given water parcel. Strong undersaturation and the associated oceanic carbon uptake are typically observed in the midlatitudes (e.g., in western boundary current extensions and the Subantarctic zone, where the net heat loss and spring/summer-time biological productivity together drive down surface pCO_2). In contrast, strong supersaturation and the associated outgassing of CO_2 are observed in the tropical upwelling regions, where the net heating and the upwelling of subsurface carbon together increase surface pCO_2. Without these physical and biological processes, the surface ocean pCO_2 would fully equilibrate with the overlying atmosphere within a few years. The Lagrangian evolution (i.e., the change observed while following the trajectory of a water parcel) of ΔC can be described by a simple differential equation,

$$\frac{\partial(\Delta C)}{\partial t} + (\mathbf{v} \cdot \nabla)(\Delta C) = -{\tau_{CO_2}}^{-1} \Delta C + f, \tag{2}$$

where τ_{CO_2} is the local gas exchange relaxation timescale for carbon dioxide and f encapsulates the physical and biogeochemical forcings that tend to generate air-sea disequilibrium (e.g., thermally induced solubility change, biological carbon uptake, and entrainment of regenerated carbon) [*Ito and Follows*, 2013]. The carbon disequilibrium ΔC is directly related to the air-sea difference in partial pressure (ΔpCO_2),

$$\frac{\Delta pCO_2}{pCO_2} = B \frac{\Delta C}{C}, \tag{3}$$

where B is the (dimensionless) Revelle Buffer factor. In a climatological and large-scale mean sense, $B \approx 10$. The observed magnitude of air-sea disequilibrium (ΔpCO_2) reflects the strength of the physical and biological forcings that work against air-sea equilibration. However, the focus of this paper is the *timescale* of air-sea equilibration (τ_{CO_2}), which can be used to understand the observed structure of ΔpCO_2. While the order of magnitude of τ_{CO_2} has been known for quite some time, its detailed spatial and temporal structure have not yet been quantified. The air-sea equilibration timescale (τ_{CO_2}) quantitatively depends on the gas transfer velocity (G), the depth of the mixed layer (h), the (dimensionless) ionization fraction (R), and the Revelle Buffer factor (B) [*Broecker and Peng*, 1974; *Ito et al.*, 2004]. This relationship can be expressed as a simple rational function:

$$\tau_{CO2} = \frac{h R}{G B}. \tag{4}$$

The ionization fraction (R) is the ratio between total carbon (C) and the dissolved CO_2 concentration, i.e., $R = C/[CO_2 *]$. The proportionality of τ_{CO_2} and R in the above equation reflects the process by which the large oceanic bicarbonate pool *slows down* air-sea equilibration relative to the equilibration timescale of inert gases (which do not interact with the bicarbonate pool). In contrast, the adjustment of the bicarbonate pool is *facilitated* by the buffering reaction via the protonation of carbonate ions:

$$CO_2 + CO_3^{2-} + H_2O \longrightarrow 2HCO_3^-. \tag{5}$$

This reaction *accelerates* the equilibration process by consuming the ambient carbonate ion (CO_3^-) and doubling the increase in bicarbonate ion per unit addition of new CO_2. Thus, the CO_2 exchange timescale scales inversely with $B \sim [HCO_3^-]/[CO_3^{2-}]$, where $B \sim O(10)$ [*Broecker and Peng*, 1974; *Sarmiento and Gruber*, 2006]. The influence of the buffer factor also explains the very slow adjustment of isotopic carbon. Since most of the dissolved inorganic carbon is composed of ^{12}C, the buffering reaction (5) does not affect the equilibration of isotopic carbon. As a result, the air-sea equilibration timescale for carbon isotopes is significantly *longer* than that of carbon dioxide by an order of magnitude, and its timescale can be calculated as follows:

$$\tau_{\mathrm{isotope}} = \frac{h R}{G}. \tag{6}$$

The gas transfer coefficient (which is normalized by the Schmidt number) essentially depends on the degree of turbulence in the surface water. However, its dependence on the surface wind speed is still uncertain and has been a subject of intense research. Early studies of air-sea gas transfer estimated the magnitude

of G using radon-222 observations [*Peng et al.*, 1979]. A number of methods have been developed to calibrate the gas transfer coefficient using the measurements of natural and bomb-induced radiocarbon [*Wanninkhof*, 1992; *Sweeney et al.*, 2007], deliberately released tracers [*Watson et al.*, 1991], and eddy covariance [*McGillis et al.*, 2001], though each method tends to capture different time and length scales. Each gas exchange parameterization scheme assumes that the rate of gas transfer increases with wind speed. However, stronger wind speed also deepens the mixed layer, which tends to *lengthen* the gas exchange timescale as shown in equation (4). It is not immediately obvious which effect dominates the evolution of ΔC, but measurements of mixed layer depth and wind speed are readily available. Specifically, remote measurements of the surface wind speed are available via the scatterometer on the QuikSCAT satellite, which can be used in conjunction with a gas exchange parameterization to yield spatially varying estimates of G. In addition, a global suite of autonomous floats (i.e., Argo, which has been in operation since the 2000s) has accumulated accurate measurements of temperature and salinity in the upper ocean, which can be used to determine the distribution of mixed layer depth [*Ohno et al.*, 2004; *Holte and Talley*, 2009; *Sallée et al.*, 2010]. A large-scale compilation of oceanic pCO_2 [*Takahashi et al.*, 2009], in conjunction with the climatological distribution of sea surface alkalinity [*Lee et al.*, 2006], can also be used to determine the global distribution of R and B. Therefore, at present we have just enough observationally based information to estimate the global distribution of τ_{CO_2}.

In this paper, we use a suite of observations to determine the spatial pattern and seasonal variability of the air-sea equilibration timescale. In section 2, we describe the data sources and methods. In section 3, we examine how various physical and chemical factors, as well as different gas exchange parameterizations, affect the equilibration timescale. In section 4, we discuss the implications of our results and suggest directions for future work.

2. Methods

2.1. Data Sources

We aim to quantify the mean and seasonal variability of the gas exchange relaxation timescale. In order to do so, we need estimates of the four important quantities in equation (4). The mixed layer depth h is derived from ARGO temperature and salinity float data that has been optimally interpolated onto a 1°×1° latitude-longitude grid with 58 vertical levels down to 2000 m [*Roemmich and Gilson*, 2009]. Monthly mean data from January 2004 to July 2010 (78 months in total) are used to construct both annual and seasonal mean mixed layer depth fields. Seasonal means are based on 3 month mean data (e.g., December-January-February or (DJF) for boreal winter). Potential density (σ_0) is calculated from this data set using a nonlinear equation of state referenced to mean sea level pressure, and the mixed layer depth is defined as the linearly interpolated depth at which $\sigma_0(h) = \sigma_0(0) + \Delta\sigma_c$, where $\sigma_0(0)$ is the potential density at the surface and $\Delta\sigma_c = 0.03$ kg/m^3 [*Gill*, 1982; *de Boyer Montégut et al.*, 2004].

The gas transfer coefficient G is typically parameterized as a function of 10 m wind speed and the Schmidt number of the gas tracer in question. A number of different parameterizations exist, and there is significant uncertainty as to which functional form is best constrained by the available data. Except where indicated in this paper, we use the parameterization of *Wanninkhof* [1992], which is expressed as $G = 0.31u^2(\mathrm{Sc}/660)^{-1/2}$, where u is the 10 m wind speed and Sc is the Schmidt number [*Sarmiento and Gruber*, 2006]. The Schmidt number is the ratio of the kinematic viscosity of the water and the molecular diffusivity of the gas tracer (here, we consider carbon dioxide). Other parameterizations explored in latter sections of this paper include that of *Liss and Merlivat* [1986], *Nightingale et al.* [2000], and quadratic and cubic functions from *Ho et al.* [2011]. Descriptions of these parameterizations are summarized in Table 1. The 10 m wind speed is obtained from two different sources, namely (i) blended data of monthly mean scatterometer winds based on QuikSCAT and National Centers for Environmental Prediction (NCEP) reanalysis from January 2000 to July 2007, and (ii) NCEP-only reanalysis monthly mean climatology [*Kalnay et al.*, 1996; *Milliff et al.*, 2004]. We primarily use the QuikSCAT/NCEP blended wind fields; the NCEP-only reanalysis is used for comparison purposes only.

To determine the carbonate chemistry coefficients, we need at least two observables from dissolved inorganic carbon (DIC), total alkalinity (ALK), pH, and pCO_2 [*Emerson and Hedges*, 2008]. For our two "known" variables, we have chosen the monthly climatology of surface ocean pCO_2 from *Takahashi et al.* [2009] and the monthly climatology of ALK from *Lee et al.* [2006]. These data are combined with the monthly

Table 1. Gas Exchange Parameterizations

Abbreviation	Equation	Reference
W92	$0.31u^2(Sc/660)^{-1/2}$	*Wanninkhof* [1992]
LM86	$\begin{cases} 0.17u(\mathrm{Sc}/600)^{-2/3}, & 0 \le u \le 3.6 \text{ m/s} \\ (2.85u - 9.65)(\mathrm{Sc}/600)^{-1/2}, & 3.6 < u \le 13 \text{ m/s} \\ (5.9u - 49.3)(\mathrm{Sc}/600)^{-1/2}, & u > 13 \text{ m/s} \end{cases}$	*Liss and Merlivat* [1986]
Nightingale	$(0.333u + 0.222u^2)(\mathrm{Sc}/600)^{-1/2}$	*Nightingale et al.* [2000]
Quadratic	$0.277u^2(\mathrm{Sc}/600)^{-1/2}$	*Ho et al.* [2011]
Cubic	$0.0283u^3(\mathrm{Sc}/660)^{-1/2}$	*Ho et al.* [2011]

climatology of sea surface temperature (T) and salinity (S) from the World Ocean Atlas 2009 [*Locarnini et al.*, 2010; *Antonov et al.*, 2010]. We first solve for the monthly climatology of pH via equilibrium carbonate chemistry. Next, we calculate the monthly climatology of the Revelle Buffer factor (B) and the ionization fraction (R). The values of B are calculated by taking the ratio between the fractional changes in pCO_2 and DIC while holding alkalinity constant locally (equation (3)). The ionization fraction (R) is then calculated using the values of pH and equilibrium constants (K_1 and K_2),

$$R = 1 + \frac{K_1}{[\mathrm{H}^+]} + \frac{K_1 K_2}{[\mathrm{H}^+]^2}. \tag{7}$$

Total alkalinity is defined following *Dickson* [1981], and the equilibrium constants are defined following *Millero* [1995]. The calculation is carried out using the CO2SYS Matlab script using seasonal and annual mean surface values of phosphate and silicate from the World Ocean Atlas 2009 data set [*Garcia et al.*, 2010; *van Heuven et al.*, 2011]. Phosphate and silicate enter into the charge balance calculation because their ionization state depends on pH (i.e., they are nonconservative ions). We use the K_1 and K_2 dissociation constants of *Millero* [2010] and the KSO_4 dissociation constants of *Khoo et al.* [1997]. Total boron is represented as a linear function of salinity following *Lee et al.* [2010].

2.2. Surface Residence Timescale

The equation for ΔC (equation (2)) suggests that the surface ΔC exponentially decays with the e-folding timescale of τ_{CO_2} in the absence of forcing (i.e., $f = 0$). In this case, the degree of air-sea equilibration is determined by the ratio between τ_{CO_2} and the surface residence time (τ_{res}), which measures how long the water parcel has been in contact with the atmosphere. It is not possible to determine τ_{res} directly from observations, but it can be estimated using a numerical ocean model.

We employ a global ocean biogeochemistry model based on the Massachusetts Institute of Technology General Circulation Model (MITgcm) [*Marshall et al.*, 1997a, 1997b] configured for 1°×1° global topography in the longitude-latitude grid with 23 vertical levels. We simulate tracer transport in the offline mode, using precomputed circulation fields from the Estimating the Circulation and Climate of the Ocean–Global Ocean Data Assimilation Experiment product, version 3 iteration 73 [*Wunsch and Heimbach*, 2007]. At this resolution, the model cannot resolve mesoscale eddies, so their effects are parameterized using an isopycnal thickness diffusion scheme [*Gent and Mcwilliams*, 1990]. Surface mixed layer processes are parameterized using the K-Profile Parameterization (KPP) scheme [*Large et al.*, 1994].

We simulate an idealized surface age tracer to estimate the spatial distribution of τ_{res}. The tracer is initialized with zeros across the entire domain, and its source is set to unity in the mixed layer. The mixed layer is defined as the depth at which the difference between the surface density $\sigma_0(z = 0)$ and the density in the interior σ_0 is equal to $\Delta\sigma_0 = 0.03$ kg/m^3. Furthermore, an additional temperature criterion is applied such that the potential temperature difference from the surface must be less than 0.2°. Below the mixed layer, the tracer is set to zero. As such, this metric of surface age estimates the total time spent within the mixed layer as defined above. The tracer field is stepped forward with a 5 h time step using linearly interpolated fields between each month. We integrate the tracer distribution forward in time for 100 years, repeatedly cycling the climatological monthly circulation fields. The spatial distribution of τ_{res} reaches a steady state in less than 10 years. The climatology is constructed by taking an annual mean after the model reaches steady state.

Numerical experiments like this one complement existing "age of water" and ventilation timescale calculations, which aim to estimate the time since a given water parcel last made contact with the atmosphere [e.g., *England*, 1995]. If we imagine a simple meridional overturning circulation, then the age of a water parcel

(i.e., time since last contact with the atmosphere) and the surface residence time can be added to produce an overturning timescale (we will not attempt this here).

2.3. Lateral Transport of ΔC

The derivative of ΔC in equation (2) includes the effects of the lateral advection across surface ΔC contours. Under the influence of rapid surface currents, air-sea gas transfer may not be able to fully equilibrate the mixed layer. In order to evaluate the relative importance of lateral advection, we define a timescale associated with lateral transport, τ_{adv}. We first calculate the length scale of ΔC, starting from the magnitude of the mean ΔC (i.e., $|\Delta C|$) and the gradient of ΔC (i.e., $|\nabla(\Delta C)|$) for each grid cell and then calculate the length scale L defined as follows:

$$L = \frac{|\Delta C|}{|\nabla(\Delta C)|}. \tag{8}$$

We then divide the length scale L for ΔC by the geostrophic velocity $|\mathbf{u}|$ to calculate the timescale τ_{adv},

$$\tau_{adv} = \frac{L}{|\mathbf{u}|}. \tag{9}$$

This advective timescale is estimated by combining observations of surface currents and the spatial distribution of ΔC. The surface current, $\mathbf{u}$, can be estimated using the surface geostrophic velocity estimated from satellite altimetry data. We use the Archiving, Validation, and Interpretation of Satellite Oceanographic data (AVISO) Level 4 Absolute Dynamic Topography for climate model comparison downloaded from the NASA Jet Propulsion Laboratory website [http://podaac.jpl.nasa.gov/dataset/AVISO$_L4_DYN_TOPO_1DEG_1MO]. This data set is based on AVISO satellite products [http://www.aviso.oceanobs.com/en/] binned in 1° boxes (i.e., the latitude-longitude grid). The data set is averaged monthly and covers from October 1992 to December 2010. We use the data from January 1993 to December 2010 to construct the long-term climatology of geostrophic velocities and then linearly interpolate onto a 4 by 5° longitude-latitude grid for transport timescale calculation, which is consistent with the horizontal resolution of the ΔC data set. The spatial gradient of ΔC is estimated from the monthly distribution of ΔpCO_2 based on *Takahashi et al.* [2009]. The pattern of ΔC reflects that of ΔpCO_2 through the Revelle factor (equation (3)).

The above estimate of the lateral advection timescale does not account for Ekman transport, i.e., the velocity scale does not include the ageostrophic component of horizontal velocity. The Ekman velocity scale can be written

$$\mathbf{U}_{Ek} = \frac{\tau_{\mathbf{wind}} \times \hat{\mathbf{z}}}{\rho f D_{Ek}}, \tag{10}$$

where $\tau_{\mathbf{wind}}$ is the wind stress vector, $\hat{z}$ is the vertical unit vector, $f = 2\Omega \sin(\phi)$ is the Coriolis parameter, ρ is the density of seawater, and D_{Ek} is the Ekman layer depth. The Ekman layer depth can be estimated using the expression

$$D_{Ek} = \frac{7.6}{\sqrt{\sin(|\phi|)}} U_{wspd}, \tag{11}$$

where U_{wspd} is the surface wind speed [*Ekman*, 1905]. We use annual mean surface wind stress and surface wind speed fields from Oregon State University (http://cioss.coas.oregonstate.edu/scow/), as described in *Risien and Chelton* [2008]. The relevant timescale for surface residence time is the shorter of the two timescales, i.e., either Ekman advection or geostrophic advection produces faster lateral transport, and faster lateral transport produces shorter lateral transport timescales.

Note that in this paper we make no effort to estimate the gas exchange timescale for a specific time period, since at present the available data are incomplete and in some cases nonoverlapping. Instead, we focus on long-term averages and seasonal composites. As such, our results should not be taken to represent a definite year or number of years, but they should instead be interpreted as long-term (and seasonal composite) averages that can be used to guide future attempts to quantify the gas exchange efficiency over more specific regions and times.

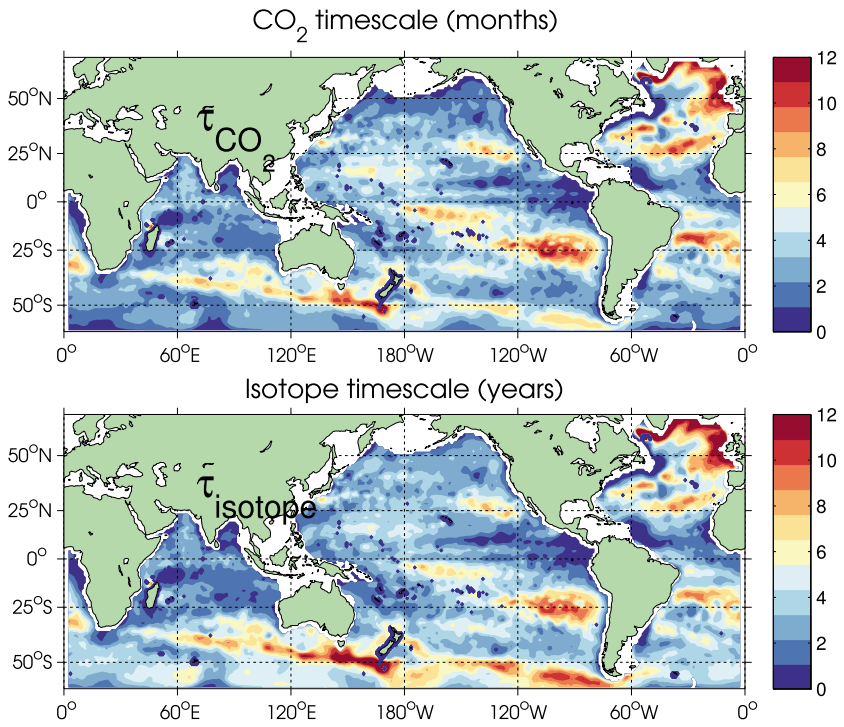

Figure 1. Map of long-term mean air-sea gas exchange adjustment timescale for (top) carbon dioxide and (bottom) carbon isotopes. White areas represent patches where data are unavailable. Note that Figure 1 (top) is shown in months, and Figure 1 (bottom) is shown in years.

3. Results

The air-sea CO_2 exchange timescale is often presented as a single, globally averaged timescale with a value of approximately 1 year, but the factors that control τ_{CO_2} all display significant spatial and temporal variability across a wide range of scales. For example, the gas exchange timescale is longer in regions of deep mixed layers and weak winds, as indicated by equation (4). In section 3.1, we first evaluate the climatological mean distribution of τ_{CO_2}, its overall spatial structure, and the uncertainties in our estimate. In section 3.2, we investigate the seasonal variability of τ_{CO_2}.

3.1. Climatological Mean

The climatological mean distribution of the air-sea equilibration timescale for carbon dioxide is shown in Figure 1 (top). The area-weighted global median τ_{CO_2} is 4.1 months, the area-weighted mean τ_{CO_2} is 4.4 months, and the area-weighted standard deviation is 3.4 months. The slight difference between the mean and median suggests that the distribution may be positively skewed (i.e., the distribution has a long tail due to the presence of several relatively small areas with long gas exchange timescales). The timescale τ_{CO_2} ranges from 0.5 months to 24 months, with especially long values in a few specific locations (e.g., the northern North Atlantic, the Atlantic subtropical gyres, and the Southern Ocean south of Australia and New Zealand). In the zonal mean, the timescale τ_{CO_2} ranges from around 3 to 6 months, except north of 55°N where deep mixed layers lengthen the timescale up to 18 months.

The air-sea relaxation timescale for carbon isotopes (Figure 1, bottom) is typically an order of magnitude *longer* than the carbon dioxide timescale, although they exhibit similar spatial patterns. Specifically, more than 60% of the surface area shown in Figure 1 lies in the same quartile of both distributions. The area-weighted median gas exchange timescale for isotopes is 4.1 years, the area-weighted mean is 4.4 years, and the standard deviation is 3.5 years. The isotope exchange timescale distribution ($\tau_{isotope}$) exhibits slight positive skew. The longest timescales are seen in roughly the same geographical locations for τ_{CO_2} and $\tau_{isotope}$. By definition, the only difference between the two timescales is the buffer factor B, so the similarity of the two distributions suggests that B is not a major driver of spatial variability in the climatological mean.

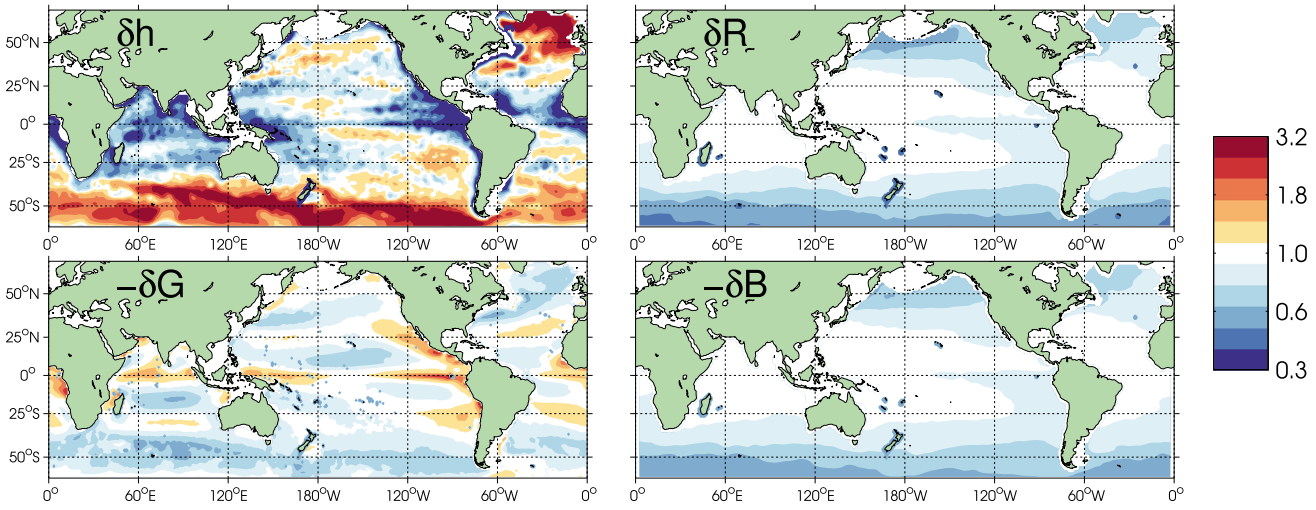

Figure 2. Relative importance of h, R, G, and B in setting spatial variability in the long-term mean gas exchange adjustment timescale. The variations are expressed as logarithmic changes (i.e., $\delta f \equiv \log_{10}(f/f_0)$) relative to global, area-weighted median values $h_0 = 37$ m, $R_0 = 194$, $G_0 = 18.8$ cm/h, and $B_0 = 11.0$. The sign of each term has been chosen such that positive (negative) values are consistently associated with lengthening (shortening) of the air-sea gas adjustment timescale in each panel.

To better understand what controls the spatial structure of the climatological air-sea gas exchange timescale, we examine the relative contributions of h, R, G, and B to the mean. The contribution of each factor to τ_{CO_2} can be expressed as a logarithmic change of the form $\delta f \equiv \log_{10}(f/f_0)$, such that deviations from the timescale around a reference value can be written as $\delta\tau_{CO_2} = \delta h + \delta R - \delta G - \delta B$, where $\tau_{CO2,0}$, h_0, R_0, and G_0 are reference values that can either be constants or some other suitably chosen fields (e.g., climatological mean maps). We express deviations as logarithmic changes (instead of using a simple linear approximation) because the nonlinearities are large relative to the linear terms in some regions. The sign of each term indicates its tendency to increase or decrease the air-sea equilibration timescale, e.g., increases in mixed layer depth tend to lengthen the timescale, while increases in the gas transfer velocity tend to *shorten* the gas exchange timescale.

In Figure 2, we plot the logarithmic deviations of the climatological mean mixed layer depth (δh), gas transfer coefficient (δG), ionization fraction (δR), and buffer factor (δB), relative to the global, area-weighted median reference values $h_0 = 38$ m, $R_0 = 188$, $G_0 = 18.9$ cm/h, and $B_0 = 11.1$. In the figure, the logarithmic changes δG and δR are multiplied by (−1) such that positive (negative) values consistently indicate a tendency for a given factor to lengthen (shorten) the adjustment timescale in each panel. Over much of the ocean's surface, mixed layer depth is the primary factor controlling the spatial pattern of τ_{CO_2}, increasing by nearly an order of magnitude from the tropics to the poles in the zonal mean. The broad pattern of shallow mixed layers in the tropics and subtropics and deeper mixed layers at high latitudes contributes to *shorter* timescales in the tropics and *longer* timescales at high latitudes. The mixed layer is exceptionally deep in the high North Atlantic and around the Southern Ocean (both important sites of deep water mass formation), so we may expect to see exceptionally long gas exchange timescales in those regions as well. The high northern latitudes are characterized by timescales that are about 2.5 times *longer* than in the Southern Ocean in the zonal mean, set by mixed layers that are 1.3 times deeper, values of R that are 30% larger, and values of B that are 25% smaller than their Southern Ocean values.

Over much of the ocean's surface, the other three factors in the gas exchange timescale (i.e., R, B, and G) only partially compensate for the influence of mixed layer depth on variations in τ_{CO_2}. The gas transfer coefficient G tends to be small at low latitudes and larger at high latitudes, increasing by roughly a factor of 1.2–2.0 in the zonal mean. Higher gas transfer velocities can partially compensate for deeper mixed layers, since strong winds encourage rapid equilibration while deep mixed layers inhibit equilibration. The air-sea equilibration timescale is inversely proportional to the gas transfer coefficient, therefore the observed pattern in G contributes to shorter timescales at midlatitude and high latitude compared to the tropics. The ionization fraction R tends to be around 1.5–2.0 times *smaller* at high latitudes than in the tropics and subtropics, contributing to shorter gas exchange timescales at high latitudes. The buffer factor B shows the opposite

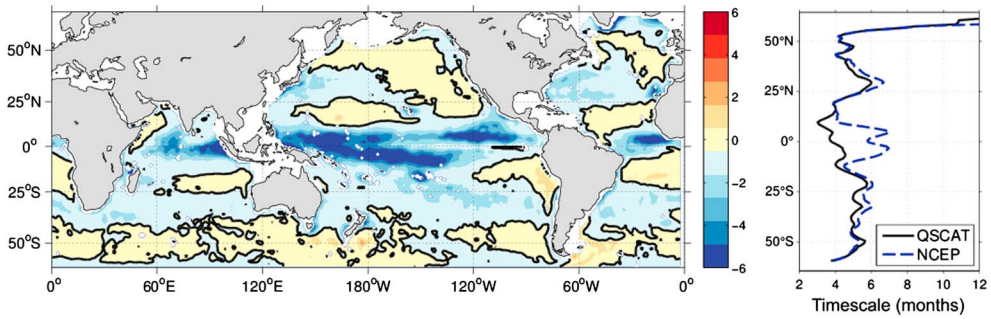

Figure 3. The difference in τ_{CO_2} due to the surface wind product derived from the NCEP reanalysis relative to the scatterometer wind field. On the left is a long-term mean map of QSCAT-NCEP timescales, and on the right are zonal means of each timescale. On the left, the thick black line marks the contour of "no difference" between the two estimates. All timescales are shown in months.

pattern, increasing with latitude by a factor of 1.4–1.8 in the zonal mean. Since τ_{CO_2} is inversely proportional to *B*, this increase in the buffer factor with latitude tends to shorten the gas exchange timescale. Together, the variations in *R* and *B* act to set a poleward *decrease* in τ_{CO_2} of about 40%, which partially offsets the tendency for deeper mixed layers to set longer gas exchange timescales. Based on the above changes in *h*, *R*, *G*, and *B* with latitude, we expect about a factor of 2 change in the zonal mean gas exchange timescale. The exception to this trend is in the high northern Atlantic, where deep mixed layers further lengthen the timescale.

Errors in the surface wind speed may affect our estimates. We primarily rely on remotely sensed scatterometer winds from QuikSCAT, but for comparison purposes we also estimate τ_{CO_2} using 10 m winds from the NCEP reanalysis [*Kalnay et al.*, 1996]. Figure 3a shows the difference between τ_{CO_2} produced using these two wind products (QuikSCAT minus NCEP), with the zero contour shown as a thick black line. For both products we use the standard gas transfer parameterization of *Wanninkhof et al.* [2009]. The largest differences are in the tropics (i.e., between 10°S and 10°N), where the climatological NCEP wind is weaker than the scatterometer wind. The error in the wind lengthens the gas exchange timescale by about 2 months in the tropics, but these particular wind products give similar results in the middle and high latitudes [*Goswami and Sengupta*, 2003]. Figure 3b shows the zonal mean values of the two products, which again show the greatest differences in low latitudes. The differences can introduce errors in the latitudinal gradient of zonal mean τ_{CO_2}.

Another significant source of uncertainty in our analysis is the gas transfer velocity parameterization; several options exist, and the individual parameterizations tend to be best suited to the particular spatial and velocity scales on which they have been observationally constrained. Figure 4 shows the zonal mean τ_{CO_2} based on several different gas transfer velocity parameterizations. Excluding the northernmost 10° in the zonal mean (where the mixed layers are exceptionally deep), the individual estimates of τ_{CO_2} all vary with latitude by roughly a factor of two, which is consistent with our earlier estimate discussed above. We find somewhat shorter timescales at lower latitudes, longer timescales at higher latitudes, and exceptionally high timescales at the northernmost latitudes. The spread of τ_{CO_2} (i.e., the ratio of LM86 and W92) produced by the various parameterization schemes tested here is about a factor of 1.5–1.8 depending on latitude, and the schemes all produce roughly the same structure of τ_{CO_2} with

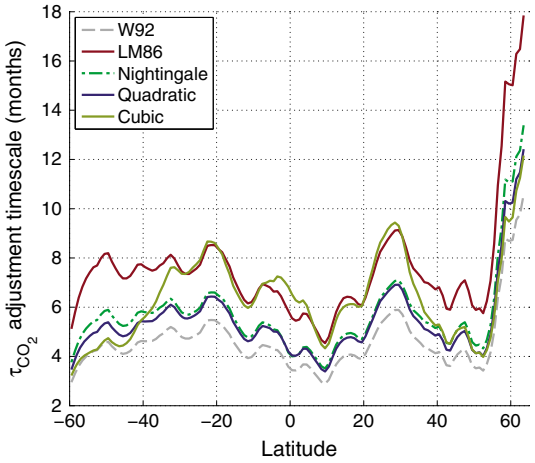

Figure 4. Zonal mean τ_{CO_2} based on several parameterizations of the gas transfer coefficient in months. W92 = *Wanninkhof* [1992]; LM86 = *Liss and Merlivat* [1986]; Nightingale = *Nightingale et al.* [2000]; and quadratic and cubic are from *Ho et al.* [2011].

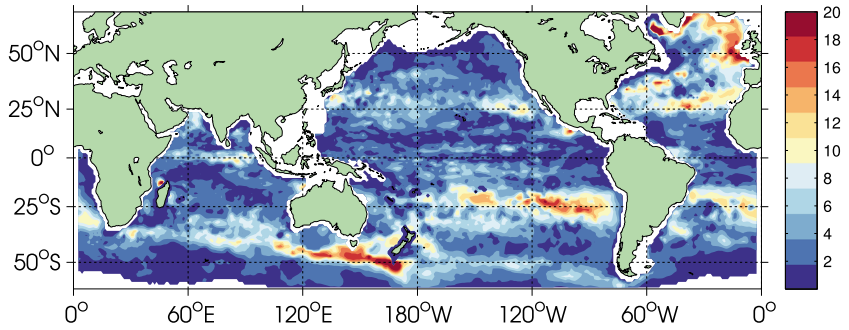

Figure 5. Amplitude of the seasonal cycle of the equilibration timescale, given in months. The amplitude is defined by comparing the four seasonal composites and calculating the difference between the maximum and the minimum timescale at each grid cell. As such, this amplitude only captures broad seasonal variations.

latitude. The exception to this trend is the cubic parameterization of *Ho et al.* [2011], which is more sensitive to wind stress than the other schemes. In this case, the increase in G with latitude overwhelms the variation in mixed layer depth. The variation of τ_{CO_2} under the cubic parameterization nearly spans the entire range of values predicted by the longest and shortest estimates (LM86 and W92, respectively). Note that the default parameterization scheme used in this paper [i.e., *Wanninkhof*, 1992] consistently produces the shortest estimates of τ_{CO_2} relative to the other schemes used in this work.

3.2. Seasonal Cycles

Both the mixed layer depth and the gas transfer velocity exhibit strong seasonal cycles; therefore, the air-sea equilibration timescale may exhibit significant variations with season as well. It is interesting to note that in some regions the timescale is *longer* than the length of a season (or even longer than a year), which introduces a lag between seasonal forcing and response. A lag implies that equilibration may not occur in regions with long adjustment timescales. This is especially true for the isotopes, with associated adjustment timescales on the order of years to decades. In Figure 5, we plot contours of the seasonal amplitude (i.e., the maximum versus the minimum gas exchange timescale at each grid cell). The (area-weighted) median amplitude is 3.3 months, and the mean amplitude is 7.5 months; the skew of around 0.9σ indicates that the amplitude distribution is skewed toward longer values, much like the long-term mean distribution. The spatial pattern of the seasonal amplitude broadly resembles that of the long-term mean; around 54% of the analyzed surface area lies in the same quartile of both (i) the seasonal amplitude and (ii) the long-term mean distributions.

As with the climatological map, our choice of gas exchange parameterization introduces some uncertainty. Among the choices used here (see Table 1), the "default" parameterization (W92) tends to produce the lowest values of the seasonal amplitude. The piecewise parameterization (LM86) tends to produce the highest values of the amplitude, ranging from 1 to 4 months longer over most of the domain and up to 9 months higher in the northern North Atlantic (i.e., north of 60°N).

In Figure 6, we plot zonal mean τ_{CO_2} by season. The largest variations are found north of 57°N, where the seasonal changes (i.e., the difference between the maximum and minimum value of the seasonal mean timescale at each latitude) in the timescale can be as large as 12 months. This amplitude roughly a factor of 3 longer than that seen in the Southern Ocean. In the midlatitudes (i.e., south of 50°N excluding the tropics), the seasonal changes can be as large as 8 months, peaking at −21.5°N and 27.5°N. Broadly speaking, τ_{CO_2} tends to be a factor of 2 longer in the winter hemisphere than in the summer hemisphere.

The seasonal variability of τ_{CO_2} is largely set by variations in mixed layer depth, though it is partially offset by changes in the gas exchange velocity. In Figure 7, we plot the zonal mean logarithmic change with season of the four factors controlling the timescale (i.e., δh, δR, δG, and δB) relative to climatological mean values at each grid point [e.g., $h_0 = h_0(x, y)$]. This approach highlights departures from local mean values, which allows us to focus on temporal rather than spatial variations. Note that since the timescale is *inversely* proportional to the gas exchange velocity (G) and the buffer factor (B), we plot the *negative* logarithmic fractional changes $-\delta G$ and $-\delta B$. The mixed layer effect is overwhelming, and it is only partially offset by changes in the zonal mean gas transfer velocity.

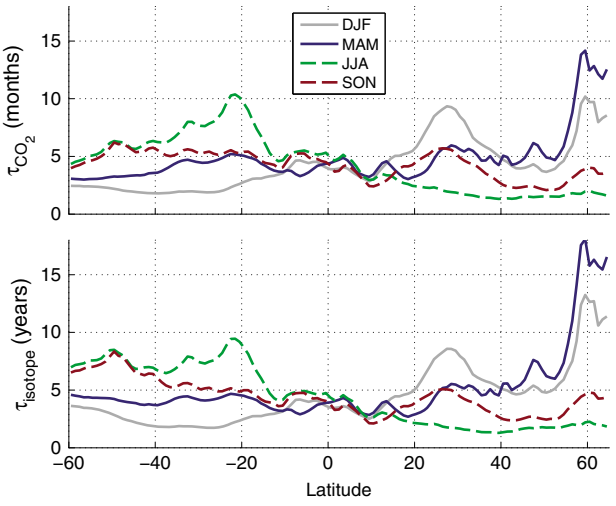

Figure 6. Seasonal cycle of the zonal mean gas exchange timescale (top) for CO_2 and (bottom) for carbon isotopes. Note that the two timescales are shown in different units.

We can quantify the degree to which a change in a given variable "explains" the observed change in the gas exchange timescale by scaling each fractional change by $\delta\tau_{CO_2}$. This is reasonable since

$$\delta\tau_{CO_2} = \delta h + \delta R - \delta G - \delta B. \quad (12)$$

For example, at 40°S in austral summer, the first-order balance is between the mixed layer depth and gas exchange velocity terms, which are approximately $\delta h/\delta\tau = 1.3$ and $\delta G/\delta\tau = 0.3$. Since these two factors have opposite sign in equation 12, they approximately sum to unity. The carbonate chemistry terms (i.e., $\delta R/\delta\tau$ and $\delta B/\delta\tau$) sum to zero, since each has a value of about 0.02. We might say that $\delta h/\delta\tau$ and $\delta G/\delta\tau$ balance at first order, while $\delta R/\delta\tau$ and $\delta B/\delta\tau$ balance at second order. At 40°S, the fractional change in mixed layer depth (δh) is about 40% *larger* than the fractional change in the gas exchange timescale ($\delta\tau$), so the gas exchange velocity must be acting in the opposite direction. Again, the seasonal changes in carbonate chemistry have little impact on τ_{CO_2} relative to the effects of mixed layer depth and wind speed variations; they typically deviate from climatological mean values at each grid cell by less than 13%. As a result, the pattern of seasonal variability is very similar for CO_2 and carbon isotopes, since the only difference between the two is a factor of B (see Figure 6). Across all latitudes and seasons, the area-weighted median values of the four factors are $\delta h/\delta\tau = 1.2$, $\delta R/\delta\tau = 0.1$, $\delta G/\delta\tau = 0.4$, and $\delta B/\delta\tau = 0.01$. This again confirms that h and G largely set the temporal variations; the carbonate chemistry parameters R and B have relatively weak seasonal variability and have a relatively small impact on the seasonal cycle of τ_{CO_2}.

3.3. Air-Sea Equilibration Efficiency

Our analysis indicates that there are regions where the gas exchange timescale is much longer than the seasonal cycle, such that there is a significant lag between forcing (e.g., seasonal buoyancy fluxes that alter the solubility of CO_2) and response (equilibration). However, equilibration is also affected by the length of time that a water parcel stays in contact with the surface. A parcel that stays in contact with the atmosphere for a *short* time relative to the equilibration timescale will *not* come to equilibrium with the overlying

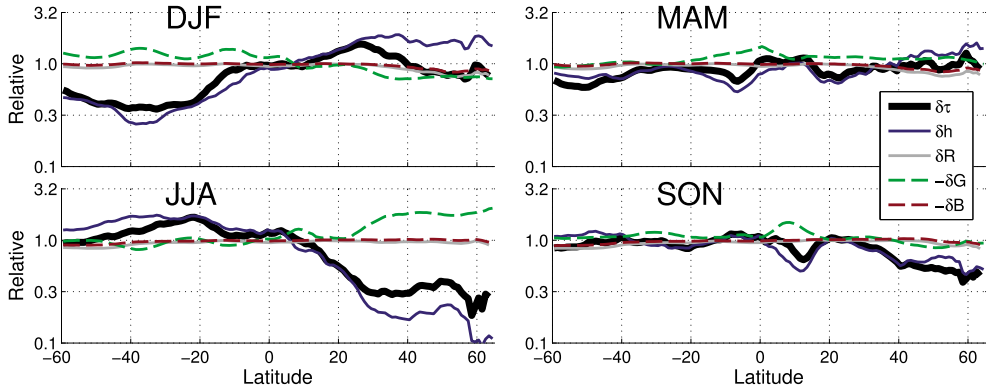

Figure 7. Seasonal averages of zonal mean logarithmic deviations [i.e., $\delta f \equiv \log_{10}(f/f_0)$] of the gas exchange timescale and the four factors used to calculate it. Changes are expressed as logarithmic deviations from the climatological fields $h_0 = h_0(x, y)$ and so on. This approach highlights temporal variability in the four fields. Note that the deviations in gas exchange velocity and buffer factor are multiplied by (−1), such that the sign of each term consistently indicates its tendency to lengthen or shorten the gas exchange timescale in each panel.

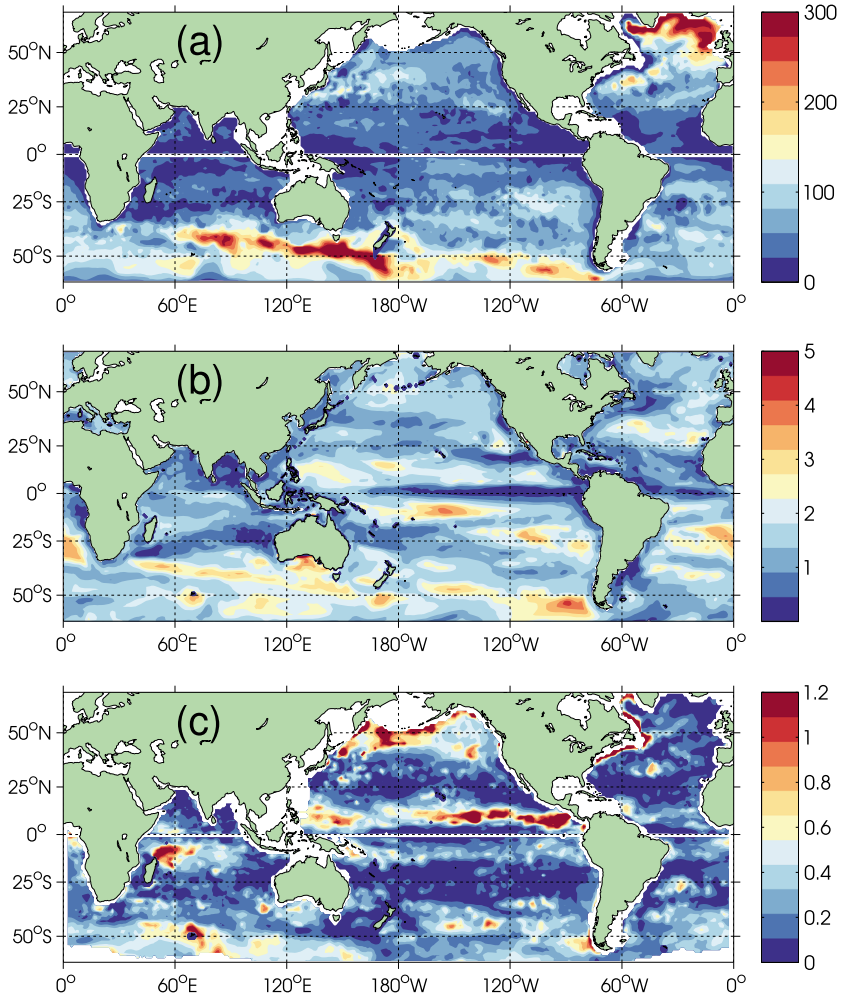

Figure 8. (a) Winter mixed layer depth (m) from ARGO gridded data, i.e., DJF in the Northern Hemisphere and June-July-August in the Southern Hemisphere. (b) The mixed layer residence time (τ_{res}, in months) as simulated by the numerical integration. (c) Spatial distribution of the equilibration efficiency parameter $\eta_{res} = \tau_{res}/\tau_{CO_2}$, where τ_{CO_2} is the wintertime value of the gas exchange timescale.

atmosphere. In this section, we estimate two transport timescales that may affect the degree of equilibration achieved by a water parcel, i.e., the surface residence time and the lateral advection timescale.

We estimate the surface residence time (τ_{res}) using observationally constrained ocean general circulation fields as discussed in section 2. The area-weighted mean τ_{res} is about 1.6 months, and the area-weighted median is roughly 1.5 months. Residence times tend to be short in the tropics (e.g., 10–12 days in the Eastern Tropical Pacific) due to shallow mixed layers and strong equatorial currents. Residence times are also short in the western boundary currents (e.g., 20–30 days in the Gulf Stream) due to rapid transport and strong mixing. In contrast, the longest surface residence times are typically found in the areas with deep winter mixed layers, especially in the Southern Indian and Southern Pacific Oceans (e.g., 3–4 months south of Australia, where the winter mixed layer is deep). Residence times are also somewhat elevated in the Atlantic subtropical gyres (e.g., 2–3 months in the North Atlantic subtropical gyre).

In order to measure the efficiency of air-sea equilibration (i.e., the relative tendency of surface waters to reach equilibrium with the atmosphere), we evaluate the ratio between the transport timescale τ_{res} and the air-sea equilibration timescale (τ_{CO_2}). That is, we define the ratio $\eta_{res} = \tau_{res}/\tau_{CO_2}$ as a simple metric of equilibration efficiency. Values of η_{CO_2} greater than 1 correspond to regions where the transport timescales are *longer* than the air-sea gas exchange timescale. In these locations, water in the mixed layer will likely have sufficient time to come to equilibrium with the overlying atmosphere before returning to the ocean interior. Values of η_{CO_2} less than one correspond to regions where the surface residence time is shorter than

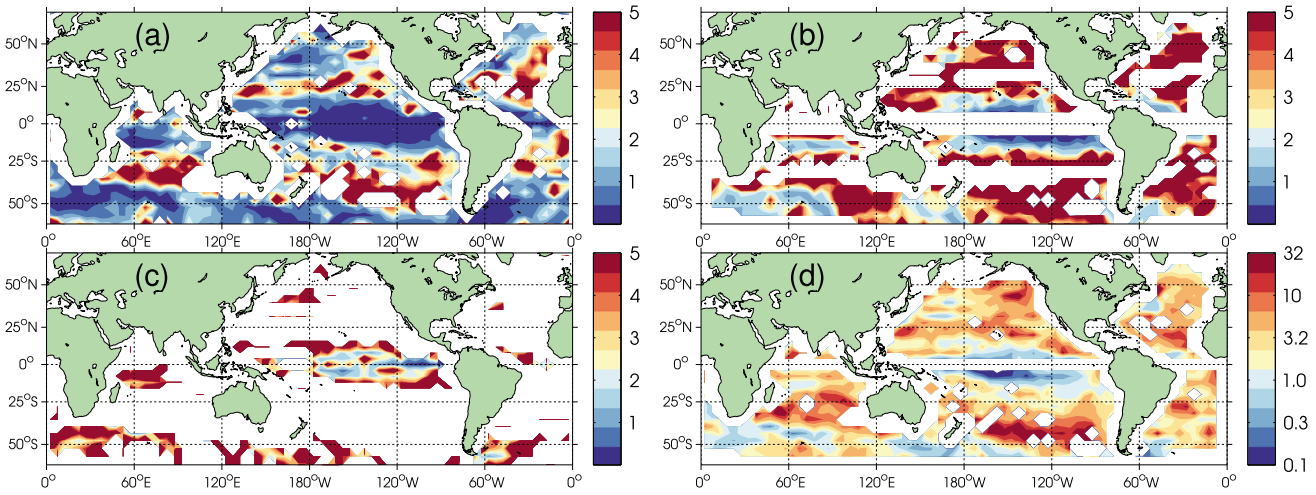

Figure 9. (a) The spatial distribution of the geostrophic lateral advection timescale (in years) estimated from the surface geostrophic current and climatological ΔpCO_2. (b) The spatial distribution of the Ekman lateral transport timescale (in years). (c) The shorter of the two lateral advection timescales (i.e., geostrophic and Ekman) (in months). Only values less than 5 months are shown in order to highlight locations of rapid lateral transport. (d) The logarithmic distribution of the equilibration efficiency parameter $\eta_{adv} = \min(\tau_{adv}, \tau_{Ek})/\tau_{CO_2}$.

the air-sea adjustment timescale. These locations of inefficient adjustment tend to favor disequilibrium if the dominant process in that region is relaxation (i.e., $f = 0$ in equation (2)).

Figure 8c shows the distribution of the relaxation efficiency $\eta_{res} = \tau_{res}/\tau_{CO_2}$. Small values of η_{res} indicate regions where relaxation is relatively ineffective at getting rid of carbon anomalies, i.e., where the surface residence time is shorter than the gas exchange equilibration timescale. Most of the ocean's surface area (over 97%) falls within the η_{res} <1 regime, which suggests that relaxation processes alone are not particularly efficient at eliminating carbon anomalies in the mixed layer. The high-latitude North Atlantic, the subtropics, and some spots in the tropics are characterized by relatively low relaxation efficiencies. In contrast, the high-latitude North Pacific, north Tropical Pacific, and Southern Oceans are characterized by relatively higher values of η_{res}. Relaxation processes encapsulated in τ_{res} should be relatively more effective at eliminating carbon anomalies in these regions. It should be noted that η_{res} is not a predictor for air-sea fluxes of carbon dioxide but rather a simple measure of how quickly anomalies decay in the mixed layer.

The surface residence time is affected by both vertical and horizontal transport. In order to quantify the importance of horizontal motion in setting equilibration, we estimate the advective geostrophic transport timescale τ_{adv} using the climatological distribution of ΔpCO_2 and sea surface topography. The results are shown in Figure 9a (shown in years). The geostrophic advective timescale is a factor of 2–3 shorter in the tropics and high latitudes compared with the central subtropical gyres compared with the tropics, which is consistent with the rapid currents found in those regions (e.g., the Antarctic Circumpolar Current and Equatorial Counter Current). In Figure 9b we plot the lateral Ekman transport timescale (in years) as diagnosed using equation (10). Although the Ekman transport timescale appears broadly similar to the geostrophic timescale, the Ekman timescale is longer than the geostrophic timescale nearly everywhere (by a factor of 4 on average). As such, Ekman transport does not significantly affect the lateral transport timescale in a long-term climatological sense. In Figure 9c, we plot the smaller of the two lateral advective timescales (i.e., geostrophic and Ekman) at each grid cell, but we omit values longer than 1 year to highlight regions where advective timescales may be important. Broadly speaking, the equatorial Pacific and a few spots in the Southern Ocean (e.g., just downstream of Drake Passage) feature particularly short advective timescales where horizontal processes may influence surface residence time.

There are some broad similarities between τ_{adv} and τ_{res}, e.g., both are relatively short in the tropics and high latitudes and are relatively long in the central subtropical gyres. However, the residence time tends to be longer than the surface age; the median advective transport timescale is roughly 3 years, whereas the median surface residence time is 1.5 months. Since the surface residence time is set by both horizontal and vertical motion (whereas the advective timescale only includes *horizontal* processes), the difference between τ_{adv} and τ_{res} indicates the degree to which vertical processes (e.g., upwelling, downwelling, and

entrainment) set the surface residence time. The difference is substantial (i.e., the advective timescales are much longer than the surface residence times), which suggests that vertical processes are more important for setting surface residence time in a large-scale sense.

Figure 9d shows the spatial distribution efficiency parameter $\eta_{adv} = \min(\tau_{adv}, \tau_{Ek})/\tau_{CO_2}$ in the common logarithm. Values of $\eta < 1$ indicate regions where advective timescales (i.e., the smallest timescale between the geostrophic and Ekman transport timescales) are shorter than the air-sea equilibration timescale of CO_2, while values of $\eta > 1$ indicate regions where advective timescales are longer than τ_{CO_2}. As discussed above, the geostrophic timescale is much shorter than the Ekman timescale nearly everywhere. The area-weighted mean η_{adv} is 3.3, and the area-weighted median value of η_{adv} is 6.5; the distribution of η_{adv} is skewed toward inefficient equilibration, though the mean and median values are well into the efficient regime. The equilibration efficiency η_{adv} is purely due to lateral advection. As such, the large values of η_{adv} seen in Figure 9d (compared with the much smaller values of η_{res} in Figure 8c) suggest that vertical processes make the global ocean less efficient at equilibrating carbon dioxide, i.e., vertical processes encourage disequilibrium with the overlying atmosphere.

4. Discussion and Conclusions

We determined the spatial and seasonal variability of the air-sea CO_2 equilibration timescale using emerging observations of mixed layer depths, wind speed, and carbonate chemistry species. Deep mixed layers and strong ionization tend to be associated with longer timescales, while rapid gas exchange rates and strong buffering tend to speed up the adjustment process. In some regions, the equilibration timescale is much longer than the seasonal forcing period, which encourages persistent anomalies in ΔC.

A recurring feature that dictates the spatial and temporal variability of τ_{CO_2} is the compensation between mixed layer depth and the gas transfer velocity. In the winter seasons, strong surface wind speeds increase the gas transfer velocity. However, the strong gas transfer rate is counterbalanced (and usually overwhelmed) by the deepening of the mixed layer. As a result, the time rate of air-sea equilibration gets weaker in the wintertime, as indicated by longer values of τ_{CO_2}. The long air-sea equilibration timescale prevents the surface waters from becoming fully equilibrated with the overlying atmosphere, producing a large air-sea carbon disequilibrium (ΔC). This has several important implications for the ocean carbon cycle.

First, note that water masses are formed at middle and high-latitude isopycnal outcrops during the winter seasons, when the mixed layer is deepest. This is precisely when air-sea equilibration is at its weakest. Thus, the preformed carbon in the newly formed thermocline and deep waters may contain large air-sea disequilibrium components. In the regions where the mixed layer gets very deep during the winter, such as in the northern North Atlantic or the subantarctic region, the degree of saturation may not strongly depend on the detailed parameterization of the gas transfer coefficient, because the surface waters may be in the weak gas exchange limit, i.e., $\tau_{CO_2} \gg \tau_{res}, \tau_{adv}$. In this case, the preformed C concentration may be controlled by the properties of the source waters that feed the subduction region.

Second, the effect of air-sea equilibration can influence the inventory and the regional distribution of the anthropogenic carbon uptake. Earlier studies [e.g., *Sarmiento and Sundquist*, 1992] showed that the magnitude of the gas transfer velocity is not the dominant factor controlling global-scale carbon uptake. *Khatiwala et al.* [2009] recently developed an inverse method to estimate the uptake of anthropogenic CO_2 that includes the effect of air-sea disequilibrium. Our results imply that there can be significant regional effects due to incomplete air-sea equilibration of anthropogenic carbon. For example, Antarctic Bottom Water, which forms in the marginal seas of the Antarctica, contains little anthropogenic carbon [*Sabine et al.*, 2004]. This may be due to the weak air-sea equilibration in the Southern Ocean, especially in the partially ice-covered polar marginal seas (see Figure 10).

Third, the incomplete air-sea equilibration can also affect the biological pump [*Ito and Follows*, 2013]. Wind-driven upwelling of deep waters, notably in the Southern Ocean, counteracts biological carbon sequestration by bringing up excess carbon from the abyss, potentially releasing it back to the atmosphere. A significant fraction of the excess carbon in the Antarctic Surface Water is not degassed to the atmosphere. Instead, it reenters the deep ocean due to incomplete air-sea equilibration, effectively increasing the biological carbon storage in the deep ocean.

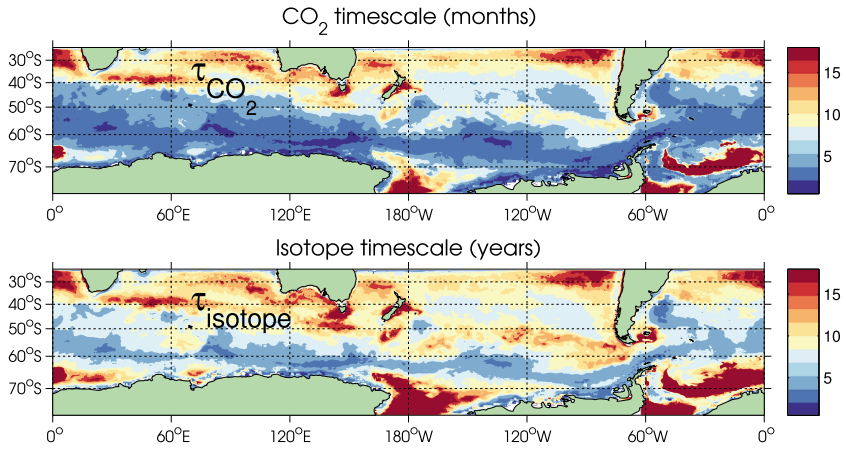

Figure 10. (top) Four-year mean equilibration timescale τ_{CO_2} (in months) derived from the Southern Ocean State Estimate (SOSE). (bottom) Four-year mean equilibration timescale $\tau_{isotope}$ (in years) estimated using SOSE fields.

Finally, in a warmer, high CO_2 climate, the stratification and carbonate chemistry of the high-latitude oceans will be different. Warming, increasing precipitation, and melting ice at high latitude likely increase upper ocean stratification, which will likely alter the depth of the mixed layer. At the same time, the area of ice-free waters may increase. Rising pCO_2 will lower the pH, which will decrease the ionization fraction (R) and increase the buffer factor (B). These shifts in carbonate chemistry may tend to shorten the air-sea equilibration timescale. Together with increased stratification and reduced ice cover, the air-sea equilibration of polar oceans may *increase* in a warming climate. The impacts of air-sea equilibration on climate change is beyond the scope of this paper, but it can potentially affect climate-carbon feedback.

Due to the limited latitude range of our mixed-layer data set, our analysis neglects processes at high latitudes. In order to partially fill in this gap, we examine 4 year mean output from a regional carbon cycle model driven by the circulation fields from the Southern Ocean State Estimate [*Ito et al.*, 2010; *Mazloff et al.*, 2010]. In Figure 10 (top), we plot the air-sea equilibration timescale for CO_2 and carbon isotopes (Figure 10, bottom) calculated from SOSE fields. The domain-averaged adjustment timescale for CO_2 is 8.8 months, a factor of 2 longer than the global mean value derived in section 3.1 from observational products. The areas of significantly longer timescales are somewhat localized, concentrated in the Ross and Weddell seas near the continent and in a few other regional spots (e.g., Tasmania and western South America). The exceptionally long timescale in the Ross and Weddell regions implies that bottom water formation there may introduce large preformed ΔC. That being said, near the Antarctic continent (excluding the Ross and Weddell seas) the equilibration timescale is anomalously *short*. This relatively short timescale is set by shallow mixed layers and the carbonate chemistry of the continental shelf waters, though it is partially mediated by weak gas exchange due to the extensive sea ice cover (see Figure 11). The balance between the four factors controlling the timescale is significantly different on the shelf from that of the open ocean. Our results indi-

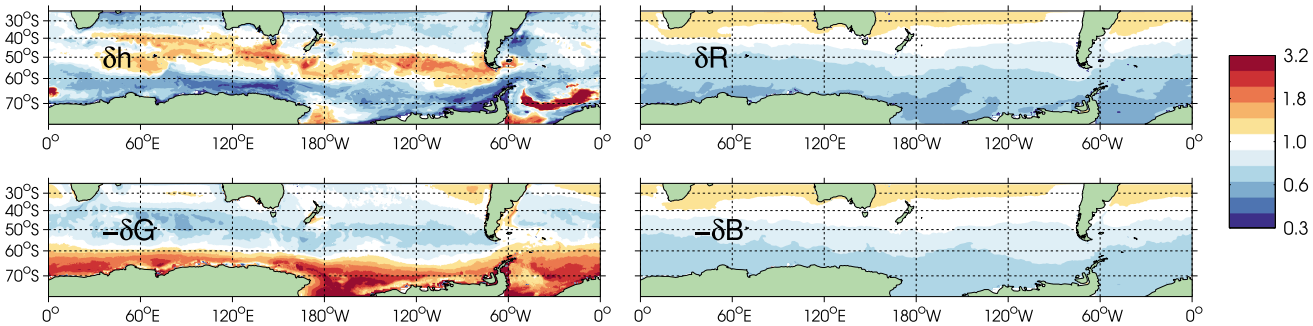

Figure 11. Relative importance of h, R, G, and B in setting spatial variability in the long-term mean gas exchange adjustment timescale. Changes are expressed as logarithmic fractional deviations about the domain-averaged, area-weighted mean values of $h_0 = 75$ m, $R_0 = 208$, $G_0 = 20.3$ cm/h, and $B_0 = 15.6$.

cate that the effect of carbonate chemistry tends to reinforce the effect of mixed layer depth off the coast of Antarctica. A full analysis of the variability of the equilibration efficiency in SOSE is left for future work.

The equilibration efficiency ratios discussed here may prove useful for understanding the behavior of complex numerical models. In order to calculate the adjustment timescale, one primarily needs the sea surface temperature, sea surface salinity, surface wind speed, and mixed layer depth, all of which are readily available in carbon-climate model simulations such as those in the Coupled Model Intercomparison Project Phase 5 archive. In order to estimate the effect of carbonate chemistry, one needs at least two of the five biogeochemical variables as described in section 2.1. Many carbon-climate models *do* simulate and archive a sufficient number of carbonate chemistry variables to quantify the air-sea adjustment timescale.

In order to better estimate the equilibration efficiency and its variability in the ocean, we need higher resolution (both spatial and temporal) observational coverage of wind speed, mixed layer depth, sea surface temperature, sea surface salinity, and a sufficient number of carbonate chemistry parameters (e.g., alkalinity, pCO_2) to allow for the full carbonate system to be solved. We also need a gas exchange parameterization scheme that can perform at high accuracy across a wide range of wind speed values. Progress in these areas will help us better understand the way in which carbon disequilibria are set and preserved in the world ocean. This should be particularly relevant at high latitudes and in the tropical Pacific, where the exchange of carbon between the atmosphere and the ocean is especially strong.

Acknowledgments

This work originates from a term project at the Georgia Institute of Technology. The authors wish to thank François Primeau, Katsumi Matsumoto, Mick Follows, Anne Willem Omta, Andrew Meijers, and an anonymous reviewer for comments that greatly improved the quality of this paper. The authors also wish to thank Emanuele Di Lorenzo for providing processed QuikSCAT data. Data analysis and visualization were carried out using Matlab R2012b and R2014b (MathWorks) and R (http://www.r-project.org/) with Rstudio (http://www.rstudio.com/). This study is part of the British Antarctic Survey Polar Science for Planet Earth Programme. The authors are grateful for support from the National Science Foundation (NSF USA, grants OCE-1242313 and OPP-1142009), the National Oceanic and Atmospheric Administration (NOAA USA, grant NA08OAR4320893), and the Natural Environment Research Council (NERC UK, grant NE/J007757/1).

References

Antonov, J. I., D. Seidov, T. P. Boyer, R. A. Locarnini, A. V. Mishonov, H. E. Garcia, O. K. Baranova, M. M. Zweng, and D. R. Johnson (2010), World Ocean Atlas 2009, in *Salinity*, vol. 2, edited by S. Levitus, 184 pp., NOAA Atlas NESDIS 69, U.S. Gov. Print. Off., Washington, D. C.

Broecker, W., and T. Peng (1974), Gas exchange rates between air and sea, *Tellus*, *26*(1–2), 21–35.

de Boyer Montégut, C., G. Madec, A. Fischer, A. Lazar, and D. Iudicone (2004), Mixed layer depth over the global ocean: An examination of profile data and a profile-based climatology, *J. Geophys. Res.*, *109*, C12003, doi:10.1029/2004JC002378.

Dickson, A. (1981), An exact definition of total alkalinity and a procedure for the estimation of alkalinity and total inorganic carbon from titration data, *Deep Sea Res., Part A*, *28*(6), 609–623.

Ekman, V. (1905), On the influence of the Earth's rotation on ocean currents, *Ark. Mat. Astron. Fys.*, *2*, 1–53.

Emerson, S., and J. Hedges (2008), *Chemical Oceanography and the Marine Carbon Cycle*, Cambridge Univ. Press, Cambridge, U. K.

England, M. (1995), The age of water and ventilation timescales in a global ocean model, *J. Phys. Oceanogr.*, *25*(11), 2756–2777.

Garcia, H., R. Locarnini, T. Boyer, J. Antonov, M. Zweng, O. Baranova, and D. Johnson (2010), World Ocean Atlas 2009, in *Nutrients (Phosphate, Nitrate, and Silicate)*, vol. 4, p. 398, NOAA Atlas NESDIS 71, U.S. Gov. Print. Off., Washington, D. C.

Gent, P., and J. Mcwilliams (1990), Isopycnal mixing in ocean circulation models, *J. Phys. Oceanogr.*, *20*, 150–155.

Gill, A. E. (1982), *Atmosphere-Ocean Dynamics*, Academic Press, Waltham, Mass.

Goswami, B. N., and D. Sengupta (2003), A note on the deficiency of NCEP/NCAR reanalysis surface winds over the equatorial Indian Ocean, *J. Geophys. Res.*, *108*(C4), 3124, doi:10.1029/2002JC001497.

Gruber, N., J. L. Sarmiento, and T. F. Stocker (1996), An improved method for detecting anthropogenic CO_2 in the oceans, *Global Biogeochem. Cycles*, *10*(4), 809–837.

Ho, D. T., R. Wanninkhof, P. Schlosser, D. S. Ullman, D. Hebert, and K. F. Sullivan (2011), Toward a universal relationship between wind speed and gas exchange: Gas transfer velocities measured with $^3HE/SF_6$ during the Southern Ocean gas exchange experiment, *J. Geophys. Res.*, *116*, C00F04, doi:10.1029/2010JC006854.

Holte, J., and L. Talley (2009), A new algorithm for finding mixed layer depths with applications to argo data and subantarctic mode water formation*, *J. Atmos. Oceanic Technol.*, *26*(9), 1920–1939, doi:10.1175/2009JTECHO543.1.

Ito, T., and M. Follows (2013), Air-sea disequilibrium of carbon dioxide enhances the biological carbon sequestration in the Southern Ocean, *Global Biogeochem. Cycles*, *27*, 1129–1138, doi:10.1002/2013GB004682.

Ito, T., J. Marshall, and M. Follows (2004), What controls the uptake of transient tracers in the Southern Ocean?, *Global Biogeochem. Cycles*, *18*, GB2021, doi:10.1029/2003GB002103.

Ito, T., M. Woloszyn, and M. Mazloff (2010), Anthropogenic carbon dioxide transport in the Southern Ocean driven by Ekman flow, *Nature*, *463*, 80–83, doi:10.1038/nature08687.

Kalnay, E., M. Kanamitsu, R. Kistler, W. Collins, D. Deaven, L. Gandin, M. Iredell, S. Saha, G. White, and J. Woollen (1996), The NCEP/NCAR 40-year reanalysis project, *Bull. Am. Meteorol. Soc.*, *77*(3), 437–471.

Khatiwala, S., F. Primeau, and T. Hall (2009), Reconstruction of the history of anthropogenic CO_2 concentrations in the ocean, *Nature*, *462*(7271), 346–349, doi:10.1038/nature08526.

Khoo, K., C. H. Culberson, and R. G. Bates (1997), Thermodynamics of the dissociation of ammonium ion in seawater from 5 to 40°C, *J. Solution Chem.*, *6*(4), 281–290, doi:10.1007/BF00645459.

Large, W., J. Mcwilliams, and S. Doney (1994), Oceanic vertical mixing: A review and a model with a nonlocal boundary layer parameterization, *Rev. Geophys.*, *32*(4), 363–403.

Lee, K., L. T. Tong, F. J. Millero, C. L. Sabine, A. G. Dickson, C. Goyet, G.-H. Park, R. Wanninkhof, R. A. Feely, and R. M. Key (2006), Global relationships of total alkalinity with salinity and temperature in surface waters of the World's Oceans, *Geophys. Res. Lett.*, *33*(19), L19605, doi:10.1029/2006GL027207.

Lee, K., T.-W. Kim, R. H. Byrne, F. J. Millero, R. A. Feely, and Y.-M. Liu (2010), The universal ratio of boron to chlorinity for the north Pacific and north Atlantic Oceans, *Geochim. Cosmochim. Acta*, *74*(6), 1801–1811, doi:10.1016/j.gca.2009.12.027.

Liss, P., and L. Merlivat (1986), Air-sea gas exchange rates: Introduction and synthesis, in *The Role of Air-Sea Exchange in Geochemical Cycling,* edited by P. Bua-Ménard, pp. 113-127, D. Reidel, Dordrecht, Netherlands, doi:10.1007/978-94-009-4738-2_5.

Locarnini, R. A, A. V. Mishonov, J. I. Antonov, T. P. Boyer, H. E. Garcia, O. K. Baranova, M. M. Zweng, and D. R. Johnson (2010), World Ocean Atlas 2009, in *Temperature*, vol. 1, edited by S. Levitus, p. 184, NOAA Atlas NESDIS 68, U.S. Gov. Print. Off., Washington, D. C.

Marshall, J., A. Adcroft, C. Hill, and L. Perelman (1997a), A finite-volume, incompressible Navier stokes model for studies of the ocean on parallel computers, *J. Geophys. Res.*, *102*(C3), 5753–5766.
Marshall, J., C. Hill, L. Perelman, and A. Adcroft (1997b), Hydrostatic, quasi-hydrostatic, and nonhydrostatic ocean modeling, *J. Geophys. Res.*, *102*(C3), 5733–5752.
Mazloff, M., P. Heimbach, and C. Wunsch (2010), An eddy-permitting Southern Ocean state estimate, *J. Phys. Oceanogr.*, *40*, 880–899, doi:10.1175/2009JPO4236.1.
McGillis, W., J. Edson, J. Hare, and C. Fairall (2001), Direct covariance air-sea CO_2 fluxes, *J. Geophys. Res.*, *106*(C8), 16,729–16,745.
Millero, F. (1995), Thermodynamics of the carbon dioxide system in the oceans, *Geochim. Cosmochim. Acta*, *59*(4), 661–677, doi:10.1016/0016-7037(94)00354-O.
Millero, F. (2010), Carbonate constants for estuarine waters, *Mar. Freshwater Res.*, *61*(2), 139–142, doi:10.1071/MF09254.
Milliff, R., J. Morzel, D. B. Chelton, and M. H. Freilich (2004), Wind stress curl and wind stress divergence biases from rain effects on qscat surface wind retrievals, *J. Atmos. Oceanic Technol.*, *21*(8), 1216–1231.
Nightingale, P., G. Malin, C. S. Law, A. J. Watson, P. S. Liss, M. I. Liddicoat, J. Boutin, and R. C. Upstill-Goddard (2000), In situ evaluation of airsea gas exchange parameterizations using novel conservative and volatile tracers, *Global Biogeochem. Cycles*, *14*(1), 373–387, doi:10.1029/1999GB900091.
Ohno, Y., T. Kobayashi, N. Iwasaka, and T. Suga (2004), The mixed layer depth in the North Pacific as detected by the ARGO floats, *Geophys. Res. Lett.*, *31*, L11306, doi:10.1029/2004GL019576.
Peng, T., W. Broecker, G. Mathieu, and Y. Li (1979), Radon evasion rates in the Atlantic and Pacific Oceans as determined during the GEOSECS program, *J. Geophys. Res.*, *84*(C5), 2471–2486.
Risien, C., and D. Chelton (2008), A global climatology of surface wind and wind stress fields from eight years of QuikSCAT scatterometer data, *J. Phys. Oceanogr.*, *38*, 2379–2413, doi:10.1175/2008JPO3881.1.
Roemmich, D., and J. Gilson (2009), The 2004–2008 mean and annual cycle of temperature, salinity, and steric height in the global ocean from the Argo program, *Prog. Oceanogr.*, *82*(2), 81–100.
Sabine, C., et al. (2004), The oceanic sink for anthropogenic CO_2, *Science*, *305*, 367–371, doi:10.1126/science.1097403.
Sallée, J., K. G. Speer, and S. R. Rintoul (2010), Zonally asymmetric response of the Southern Ocean mixed-layer depth to the Southern Annular Mode, *Nat. Geosci.*, *3*, 273–279, doi:10.1038/NGEO812.
Sarmiento, J. L., and N. Gruber (2006), Ocean Biogeochemical Dynamics.
Sarmiento, J. L., and E. Sundquist (1992), Revised budget for the oceanic uptake of anthropogenic carbon dioxide, *Nature*, *356*, 589–593.
Sweeney, C., E. Gloor, A. Jacobson, R. M. Key, G. McKinley, J. L. Sarmiento, and R. Wanninkhof (2007), Constraining global air-sea gas exchange for CO_2 with recent bomb 14C measurements, *Global Biogeochem. Cycles*, *21*, GB2015, doi:10.1029/2006GB002784.
Takahashi, T., et al. (2009), Climatological mean and decadal change in surface ocean pCO_2, and net sea-air CO_2 flux over the global oceans, *Deep Sea Res., Part II*, *56*, 554–577, doi:10.1016/j.dsr2.2008.12.009.
Toggweiler, J., A. Gnanadesikan, S. Carson, R. Murnane, and J. Sarmiento (2003a), Representation of the carbon cycle in box models and GCMS: 1. Solubility pump, *Global Biogeochem. Cycles*, *17*(1), 1026, doi:10.1029/2001GB001401.
Toggweiler, J., R. Murnane, S. Carson, A. Gnanadesikan, and J. L. Sarmiento (2003b), Representation of the carbon cycle in box models and GCMs: 2. Organic pump, *Global Biogeochem. Cycles*, *17*(1), 1027, doi:10.1029/2001GB001841.
van Heuven, S. V., M. Hoppema, A. Velo, H. J. W. D. Baar, and S. Khatiwala (2011), *Storage of C-ant in the South Atlantic Ocean. A Comparison of Results From Various Methods,* The Ocean Carbon Cycle at a Time of Change: Synthesis and Vulnerabilities, 14-16 September 2011, UNESCO, Paris, France.
Wanninkhof, R. (1992), Relationship between wind speed and gas exchange, *J. Geophys. Res.*, *97*(25), 7373–7382.
Wanninkhof, R., W. E. Asher, D. T. Ho, C. Sweeney, and W. R. McGillis (2009), Advances in quantifying air-sea gas exchange and environmental forcing, *Annual Rev. Mar. Sci.*, *1*, 213–244.
Watson, A., P. Liss, and R. Duce (1991), Design of a small-scale in situ iron fertilization experiment, *Limnol. Oceanogr.*, *36*(8), 1960–1965.
Wunsch, C., and P. Heimbach (2007), Practical global oceanic state estimation, *Physica D*, *230*(1), 197–208.